Jet Noise Prediction using Hybrid RANS/LES with Structured Overset Grids

Jeffrey A. Housman*[1], Gerrit-Daniel Stich†[2], Cetin C. Kiris*[1]
and James Bridges‡[3]

[1]*NASA Ames Research Center, M/S 258-2, Moffett Field, CA 94035*

[2]*Science and Technology Corporation, M/S 258-2, Moffett Field, CA 94035*

[3]*NASA Glenn Research Center, Lewis Field, Cleveland, Ohio 44135*

Hybrid RANS/LES simulations using the structured overset grid approach and a low-dissipation finite-difference method within the Launch Ascent and Vehicle Aerodynamics (LAVA) solver framework are presented for jet noise prediction. The simulations are part of a validation effort to demonstrate jet noise prediction capability, to assess noise characteristics of next generation quiet supersonic commercial jets. Results are compared with experimental data acquired in the Small Hot Jet Acoustic Rig in the Aeroacoustic Propulsion Laboratory at NASA Glenn Research Center. Details of the structured overset grids, numerical discretization, and turbulence model are provided. Near-field comparisons to PIV data and far-field comparisons to microphone data are discussed. Excellent agreement of time-averaged mean quantities along the jet center-line and lip-line are obtained. Good agreement with root-mean-squared (RMS) quantities along the jet center-line are also obtained. An over prediction of lip-line RMS at the nozzle exit is observed leading to a small over-prediction of side-line far-field noise (less than 2 dB) . Good agreement with far-field noise in the Mach wave radiation directions is achieved.

I. Introduction

An effort to develop a quiet supersonic business jet has been initiated at the National Aeronautics and Space Administration (NASA). The return of commercial supersonic flight will allow passengers to travel over the continental U.S. within a few hours, and an international business trip could be completed in a single day. Recently, NASA awarded a contract for the preliminary design of a "low boom" flight demonstrator aircraft for the Quiet Supersonic Technology (QueSST) project. In order to reduce or eliminate the sonic boom ground signature, several modifications to the airframe are necessary. These include increased sweep of the wing, a much longer and slender fuselage, as well as several modifications to both the design and placement of the engines. Although the focus of the design is currently being placed on reducing the ground signature at supersonic cruise, in order for the airplane to be certified (assuming the FAA eventually allows over-land supersonic flight), it must also satisfy noise constraints during takeoff and landing when the aircraft is traveling at subsonic speeds. Computational aeroacoustic simulation tools can be used to assess the new designs at these lower speeds. This work represents the first part of a systematic validation effort to demonstrate the jet noise prediction capabilities of the Launch Ascent and Vehicle Aerodynamics (LAVA) solver framework.[1]

Jet noise predictions using CFD have been reported for more than four decades. A review of the methods and accuracy of the simulations prior to 2008 is described in Bodony and Lele.[2] Much has improved over the last decade including high-fidelity simulations approaching flight Reynolds numbers, as well as inclusion of important geometric features such as the wing and nacelle, jet-ground impingement noise, and preliminary models including fan and guide vane effects.[3–8] Many of the simulations reported in the literature rely on wall-modeled Large Eddy Simulation (LES) and are still limited to simple geometries, and Reynolds

*Computational Aerosciences Branch, NAS Division, AIAA Senior Member

†Computational Aerosciences Branch, NAS Division, AIAA Member

‡Acoustics Branch, NASA Glenn Research Center, Associate Fellow AIAA

numbers that are a factor of two to ten smaller than realistic Reynolds numbers. The emphasis of this work is on demonstrating jet noise prediction capability within the LAVA framework, which can already handle complex geometry, flight Mach and Reynolds numbers, and has been used for several airframe aeroacoustic problems.[9,10] Previous jet noise prediction results using the LAVA framework focused on supersonic jets and included jet-ground[11] and jet-jet[12] impingement noise. This work focuses on free-jet noise which can be more subtle than impingement related noise.

Hybrid RANS/LES simulations using the structured overset grid approach and a low dissipation finite-difference method within LAVA are presented for jet noise prediction. In Section II, the jet noise experiments performed in the Small Hot Jet Acoustic Rig in the Aeroacoustic Propulsion Laboratory at NASA Glenn Research Center, and the data from the experiments which are used in the validation comparisons are briefly described. The computational methodology is explained in Section III, including the low dissipation finite-difference method, the hybrid RANS/LES turbulence models, and the synthetic eddy method used in this analysis. The computed results are presented in Section IV including the overset grid system, flow-field visualizations, near-field comparisons to PIV data, far-field comparisons to microphone data, and *a posteriori* error analysis of the mesh. Section V summarizes the work.

II. Problem Description

The Small Hot Jet Acoustic Rig (SHJAR), which is located in the Aeroacoustic Propulsion Laboratory (AAPL) at NASA Glenn Research Center, was commissioned in 2001 to test jet noise reduction concepts and develop advanced measurement techniques. Details of the SHJAR, the measurement techniques used to acquire the near-field and far-field data, and validation of the experimental results are presented in Refs. 13, 14. Figure 1 shows a perspective diagram of the SHJAR including the test nozzle and microphone layout on the left side of the image. Note that the nozzle axis in the downstream flow direction is marked as 180 degrees in the experimental coordinate system. The baseline axisymmetric convergent Small Metal Chevron (SMC000) nozzle, shown in Figure 2a, is the geometry used for the current test case. While Figure 2b shows the orientation of the PIV planes. The test conditions used for this study are referred to as Set Point 7 with an acoustic Mach number of $U_{jet}/c_\infty = 0.9$, a jet temperature ratio of $T_{jet}/T_\infty = 0.835$, nozzle pressure ratio of $P/P_\infty = 1.861$, a jet Mach number of $U_{jet}/c_{jet} = 0.985$, and Reynolds number of 1 million based on the nozzle diameter $D = 0.0508$ meter (2 inch). These conditions are similar to those reported in Ref. 7 , in which experiments where performed at the "Bruit et Vent" jet-noise facility of the PPRIME Institute at the Centre d'Etudes Aerodynamiques et Thermiques (CEAT). The full geometry of the nozzle (interior and exterior), including a large converging section not shown in Figure 2a, was used for the simulations. Near-field PIV data and far-field microphone data acquired in the SHJAR for Set Point 7 using the SMC000 nozzle were provided by NASA Glenn Research Center for validation.[15]

III. Computational Methodology

The LAVA solver framework[1] is utilized for the computational study. LAVA offers flexible meshing options and was developed with the intent of modeling highly complex geometry and flow-fields. The framework supports Cartesian and curvilinear structured grids as well as unstructured arbitrary polyhedral meshes. Overset grid technology[16] is used to couple the solutions across different overlapping meshes. In this study, the structured curvilinear overlapping grid methodology is applied. Best practices on mesh generation for jet noise prediction using structured multi-block grids[17] and unstructured grids[3] are expanded to structured overlapping grids in this work. The Chimera Grid Tools (CGT)[18] software package is used to generate the grids, while the hole cutting and connectivity for the overset grid system is performed within the LAVA framework.

The compressible hybrid Reynolds Averaged Navier-Stokes/Large Eddy Simulation (RANS/LES) equations are solved using a finite-difference formulation applied to the curvilinear transformed system of equations in strong conservation law form.[19] The Spalart-Allmaras (SA)[20] turbulence model is used as the base RANS closure model. Two hybrid RANS/LES modeling approaches are assessed for the jet noise simulations, including a zonal and a non-zonal formulation. Implicit second-order backward differencing is used for time integration and the discretized equations are marched in pseudo-time until a sufficient reduction in the residual has been achieved for each physical time-step (approximately 3 to 4 orders of residual reduction is achieved in the present computations). The nonlinear system of equations are linearized at each pseudo

time-step and an alternating line-Jacobi relaxation procedure is applied. Local pseudo time-stepping is used to accelerate convergence. Domain decomposition and the Message Passing Interface (MPI) are used to enable a scalable parallel algorithm.

III.A. Low Dissipation Finite-Difference Method

High-order accurate finite-difference schemes have been shown to be an effective strategy for accurately and efficiently capturing noise generation phenomenon using LAVA.[9–12] A thorough study comparing several high-order finite-difference methods on Cartesian grids within the LAVA framework was reported previously.[21] Results from this study indicated that high-order Weighted Essentially Non-Oscillatory (WENO) schemes[22] performed well in both resolution (Points-Per-Wavelength PPW), shock capturing, and robustness under harsh flow conditions. A natural extension of finite-difference WENO schemes to curvilinear grids are the high-order Weighted Compact Nonlinear Schemes (WCNS).[23] The WCNS method, applied to the convective fluxes, consists of WENO interpolation (as opposed to reconstruction) of the left and right states to the half grid points, followed by evaluation of the numerical flux at the half points by an approximate (or exact) Riemann solver or flux vector splitting scheme, and concluding with a high-order central finite-difference operator at the grid points which depends on the numerical fluxes at the half points in either an implicit (i.e. compact) or explicit form. When applying finite-difference methods to the curvilinear equations in strong conservation law form, standard WENO finite-difference methods will not satisfy the Geometric Conservation Law (GCL) making it necessary to combine the WENO interpolation with high-order central-difference operators. It has been shown that free-stream preservation (i.e. the GCL condition) is satisfied up to machine precision provided that identical central difference operators are used for discretizing the metric terms as well as the fluxes.[24,25] An additional advantage of WCNS over WENO is the ability to use approximate Riemann solvers. Standard finite-difference WENO methods require the use of flux vector splitting methods for numerical flux evaluation. In this work, a modified version of the Roe numerical flux is used.[26–28]

A consequence of using high-order central difference operators applied to numerical fluxes at the half grid points, which depend on high-order WENO interpolation, is the much wider stencil required for the same order of accuracy compared to the standard finite-difference WENO method. To reduce this pathology, high-order central difference operators using a combination of the numerical fluxes at the half grid points and the physical fluxes at the grid points have been developed.[29,30] This approach, denoted Hybrid Weighted Compact Nonlinear Scheme (HWCNS), allows for up to fifth-order accuracy using a seven-point stencil by combining fifth-order WENO interpolation with a sixth-order hybrid central difference operator. In the current approach, the convective fluxes (and the metric-terms used within) are discretized with the high-order HWCNS, while the viscous fluxes (and there metric terms) are discretized with standard second-order accurate central differencing. A more detailed description is included in Housman *et. al.*[10] In addition to the upwind biased WENO interpolation used in the HWCNS, a blending of a sixth-order centered interpolation operator is used to increase the maximum spectral resolution of the scheme. The blending factor between central and upwind biased interpolation can be based on the local Mach number at the half grid point[31] or set to a constant value (0.3 or 30 percent upwind and 70 percent central was used in the present results). The blending is only applied to the interior nozzle zones near the exit and the shear layer/jet core grids, while the upwind interpolation (which is more dissipative) is used on the highly stretched far-field grids to prevent aliasing errors and reflections.

III.B. Non-Zonal Hybrid RANS/LES model

The Detached Eddy Simulation[32,33] (DES) and Delayed Detached Eddy Simulation[34–36] (DDES) turbulence model closures are well-tested hybrid RANS/LES models for highly separated flows. In the original DES model, the transition between RANS and LES models was based strictly on local mesh size relative to the wall-distance. For geometries with a wide range of geometric length scales, such as a high-lift device with finite-thickness leading and trailing edges or nozzles with finite thickness exits, the local mesh spacing may become small enough to force transition from the RANS model to the LES model, but the mesh is typically not small enough to resolve the unsteady fluctuations causing the well-known model stress depletion.[37] This brought about the modification of the model denoted DDES which attempts to maintain RANS mode in the attached boundary layer.[34] Inspection of the shielding function often shows a strange behavior of going

from RANS near the wall, to LES, back to RANS just past the edge of the boundary layer, and subsequently back to LES.[38]

One critique of hybrid RANS/LES models is the slow development of three-dimensional turbulent structures even when the spatial and temporal resolution are more than enough to capture them. This is often caused by the definition of the local length scale in the model, which for the DDES model is the largest edge length associated with the cell (or dual cell) of a grid point. An alternative length scale definition developed using the Zonal Detached Eddy Simulation (ZDES) approach[39,40] utilizes a normalized vorticity vector together with combinations of two-dimensional length scale estimates. The normalized vorticity vector allows the span-wise or azimuthal direction to be identified in the initial onset of two-dimensional instabilities, and removes the grid length spacing in that direction (which may be large compared to the streamwise and shear directions) from the local length scale estimate. This reduction is effectively ignored once three-dimensional turbulent structures are formed. At this point the normalized vorticity vector will not be aligned with any particular mesh direction and the standard length scale is recovered. Utilization of the normalized vorticity vector along with a more conservative estimate of the mesh spacing has been developed[41] and is used in the present work. A detailed description of the length scale definition is included in Housman *et. al.*[10]

III.C. Zonal Hybrid RANS/LES model

An alternative strategy appropriate for structured multi-block and overset grids is the Zonal DES (ZDES) approach[40] in which specific zones are designated to use the RANS, DDES, or LES models explicitly. This idea of zonal specification has been further generalized to include wall distance and y^+ based transition between RANS and LES (or numerical LES).[4,42] This allows the user to choose, based on a strong understanding of the physics of the problem, which regions should be solved in pure RANS and hybrid RANS/LES mode. When in hybrid RANS/LES mode it also gives the additional freedom for the user to prescribe the transition based on wall y^+ to explicitly guarantee that the attached boundary layer remains in RANS mode. This is very important since shielding functions, such as those used in the DDES model, can still fail when the mesh is fine enough to capture some three-dimensional fluctuations, but not fine enough to resolve the largest scales in the boundary layer to predict an accurate skin friction.

In the current approach, denoted RANS-NLES (numerical LES),[4,43] the user selects which zones to solve in pure RANS mode and which zones to apply the RANS-NLES model. In the RANS-NLES zones, the user also prescribes a wall distance at which to transition from the RANS turbulent eddy viscosity to a numerical (or implicit) LES model, i.e. $\mu_T = 0$. Accuracy of the HWCNS used for numerical LES has previously been established.[44] In order to ensure that a proper turbulent eddy viscosity is used in the RANS boundary layers, the standard Spalart-Allmaras turbulence model is solved in the entire domain using a running time-average of the velocity and material properties (density and viscosity) instead of the instantaneous values. Since the unsteady hybrid RANS/LES simulations are typically started from a steady or unsteady RANS solution, the turbulent eddy viscosity is already well-established and the attached boundary layers remain relatively unchanged. A simple hyperbolic tangent function is used to modify the turbulent eddy viscosity before it is used in the viscous flux discretization,

$$\mu_T^{mod} = \left[\frac{1}{2} - \frac{1}{2}\tanh\left(\epsilon_d\left(d_{\text{wall}} - d_0\right)\right)\right]\mu_T, \tag{1}$$

where d_{wall} is the wall distance, d_0 is the user-specified transition distance location, and ϵ_d is a user-specified blending which controls how sharp the transition is between the RANS and LES models. Typically d_0 is chosen based on a y^+ criteria at a critical location in the flow with values between $50 \leq y^+ \leq 250$, and the blending parameter is chosen such that the interface is spread over $5 - 20$ grid points in the wall-normal direction. Note that the turbulent eddy viscosity used within the Spalart-Allmaras turbulence model is not overwritten by the modified version. This implies that if the time-averaged solution is identical to the steady RANS solution used to initialize the problem, then the turbulent eddy viscosity generated by the RANS turbulence model remains unchanged. This procedure is not limited to the Spalart-Allmaras model and can easily be adapted to any of the standard RANS turbulence models available in the literature. In order to assess which model is being used spatially, an indicator function, denoted f_d to be consistent with the DDES model, is defined by

$$f_d = 1 - \left[\frac{1}{2} - \frac{1}{2}\tanh\left(\epsilon_d\left(d_{\text{wall}} - d_0\right)\right)\right], \tag{2}$$

when in hybrid mode and $f_d = 0$ when in RANS mode.

III.D. Synthetic Eddy Method

The noise produced by attached boundary layers, such as the boundary layer near a nozzle exit, are highly dependent on the three-dimensional turbulent structures near the wall. These turbulent structures also significantly influence the development of the turbulent jet shear layers emanating from the nozzle exit which dictate the accuracy of the far-field acoustic prediction.[7] Non-zonal methods, such as DDES, are known to be less accurate for these types of flows, and only Direct Numerical Simulation (DNS) and wall-resolved LES are truly capable of modeling these turbulent structures deep in the boundary layer.[45] Since wall-resolved LES of even small portions of the nozzle interior, near the nozzle exit, are still not affordable for realistic Reynolds numbers, an alternative strategy must be developed. One approach is to utilize wall-modeled LES[7,46,47] which substantially reduces the meshing requirements compared to wall-resolved LES. In the current approach, the RANS-NLES model described above is used in the nozzle interior, just upstream of the nozzle exit which transitions to NLES for the jet. The d_0 parameter is chosen such that the model transitions from RANS to NLES at approximately $y^+ = 100$ based on the nozzle exit boundary layer predicted using a preliminary RANS analysis. Since no turbulent fluctuations are resolved in the pure RANS zones in upstream nozzle interior, artificial turbulent fluctuations (LES inflow) must be added at the interface between the RANS and hybrid RANS-NLES zones to facilitate the development of resolved turbulent structures in the outer-region of the boundary layer where the NLES model is activated. The Synthetic Eddy Method (SEM)[48,49] which introduces synthetic eddies at the interface, such that first and second order turbulent statistics are matched with the upstream RANS solution, is used. The eddies are convected at a characteristic velocity in order to mimic the temporal and spatial correlations of actual three-dimensional turbulence. Specification of the eddies and their downstream evolution are illustrated for a turbulent channel flow in Figure 3a. Once the governing equations are integrated forward in time for a sufficiently long duration, the turbulent statistics can be assessed. Figure 3b-d show the time-averaged stream-wise velocity, the RMS stream-wise velocity, and the resolved turbulent kinetic energy. Although the interface will converge to the correct first and second order statistics, there is a delay before physical three-dimensional turbulence is recovered. This can be observed in the RMS of the stream-wise velocity. Some modifications of the formulation have been made regarding the size of the eddies.[50] For the jet-noise simulations the SEM interface is placed approximately 53 nozzle exit boundary layer thicknesses upstream of the nozzle exit.

IV. Computational Results

High-fidelity time-accurate jet noise simulations were performed to assess the capabilities of the LAVA hybrid RANS/LES models with the low dissipation finite-difference method. Two different approaches to hybrid RANS/LES modeling were included in the analysis and the SEM method is additionally applied to one of the hybrid models. Three different overlapping grids were generated and will be described in detail below. A time-step of one microsecond is used for all of the simulations along with 5 sub-iterations which equated to $3-4$ orders of magnitude residual reduction at each physical time-step of the dual-time stepping algorithm. This time-step is equivalent to a $\Delta t^+ = 1.1$ based on the nozzle exit diameter, exit viscosity, and u_τ at the exit computed from the RANS analysis. If an explicit time-marching scheme is used with the current mesh and a CFL restriction of unity is enforced, then the time-step would need to be reduced three orders of magnitude compared to the current simulation because of the viscous wall spacing. To begin the simulations, unsteady RANS is performed at a larger time-step of 100 microseconds for a sufficiently long duration until a nearly steady-state solution is obtained. Next, the hybrid RANS/LES models were activated and $20,000$ time-steps were performed to flush-out the transients created by activating the hybrid models (this includes activation of the SEM). Finally an additional $30,000$ time-steps were performed and turbulent statistics for near-field comparisons were taken over the final $20,000$ time-steps. This is equivalent to a simulation of 342 convective time units (D_{exit}/c_∞) with statistics taken over 205 convective time units. The computer resources utilized for the different grids were 260 (Ivy Bridge) cores for 28 million grid points, 960 (Ivy Bridge) cores for 106 million grid points, and 1392 (Haswell) cores for 256 million grid points. This is equivalent to approximately $110,000-185,000$ points per core. The initial unsteady RANS simulations are run for 24 hours, then the remaining hybrid RANS/LES simulations required $7-15$ days for the $30,000-50,000$ time-steps depending on the number of points per core and the number of time-steps. Note the time over which the turbulent statistics is performed is rather small, at 0.03 seconds but consistent with others reported in the literature.[3,7]

IV.A. Structured Overset Grid System

The advantage of structured overset grids for aeroacoustic analysis of jet noise includes the ability to generate highly anisotropic grids to capture the nozzle boundary layers and shear layers and to locally refine the meshes in the azimuthal direction at different streamwise and radial locations along the jet axis. Structured grid flow solvers are also highly efficient, have a low memory footprint, and offer a straightforward and inexpensive extension to high-order low dissipation finite-difference discretizations. Allowing the structured grids to overlap each other not only simplifies the process of generating the grids (in comparison to structured multi-block abutting grids), it also allows for high quality (less-skewed) meshes. The baseline structured overlapping grid system is generated for the SMC000 nozzle following the specifications detailed in Bogey *et. al.*[17] which used structured multi-block grids. Tight-clustering is used near the viscous walls to guarantee a $y^+ \approx 1$ throughout the nozzle interior, while 51 points were used along the nozzle lip which has a thickness of 0.027 m. The fine spacing used at the nozzle lip is extended along the downstream jet axis to provide significant resolution across the shear layer of the jet in the radial direction. Square cells are used in the radial and axial directions from the nozzle exit to one nozzle radius downstream, then the axial spacing is stretched at maximum stretching ratio of 1.014 in the jet direction out to 30 D (where D is the nozzle diameter) where the aspect ratio of the axial spacing to the radial spacing is approximately 8 in the shear layer portion of the mesh. After 30 D, the mesh is stretched at a 1.2 stretching ratio to a far-field distance of 280 nozzle diameters. The three-dimensional grid is generated by rotating the two-dimensional slice 360 degrees using 361 uniformly distributed points, resulting in approximately 256 million grid points which is similar to the coarse grid generated in Bogey *et. al.*[17]

Some important benefits of varying the circumferential spacing at different axial and radial locations were reported in Ref. 7, and a coarser mesh was constructed targeting the same accuracy as the existing 256 million grid point mesh. First, a 28 million grid point structured overlapping grid was generated by relaxing the relatively fine axial grid spacing to just 25 D before stretching to a far-field distance of 60 D and by using adjustable circumferential spacing at different locations along the jet. Next, a refined mesh was generated from the coarse mesh by reducing the grid spacings throughout the mesh resulting in 106 million grid points, and used 721 points in the circumferential direction at the nozzle exit. Figure 4 plots a cutting plane through the jet centerline along with nozzle surfaces of the structured overlapping grid systems for the baseline, coarse, and refined grids. The tight clustering in the nozzle shear layers and the mild stretching in the axial spacing along the jet is observed in all three grid systems. The axial variation in circumferential spacing is illustrated on the surface mesh (shown in green) of the coarse and refined grids where finer circumferential spacing is used as the nozzle exit is approached. Figure 5 plots a streamwise cutting plane of the refined grid which shows the radial variation of the circumferential spacing. In this work, only factors of two increase/decrease are used in the circumferential spacing between grid zones which communicated overset information between each other. It should be recognized that although these grids are relatively large compared to some previous studies,[51,52] they are significantly coarser than the suggested spacings for wall-resolved or wall-modeled LES.[53,54] For example, the number of azimuthal grid points suggested in Ref. 54 for wall-modeled LES based on $\Delta s_{azimuth} = 0.05\delta^{BL}_{exit}$ is 4911 points, where δ^{BL}_{exit} is the boundary layer height at the nozzle exit computed from the RANS calculation. While the number of azimuthal grid points suggested for wall-resolved LES based on $\Delta s^+_{azimuth} = 10$ is $25,852$ points. Note these estimates may be excessive and high quality results may be achievable using LES with much coarser spacings.[3,7]

IV.B. Flow Field Visualizations

Simulating aeroacoustic phenomena requires high-resolution turbulence resolving schemes and accurate turbulence models to provide dissipation for the unresolved scales. Figures 6 (a) and (b) show instantaneous plots of the Q-criteria colored by normalized axial velocity and the magnitude of the density gradient on a cutting plane through the jet using the DDES model on the baseline grid. The merging of the three-dimensional turbulent structures in the jet shear layer at the end of the potential core and the acoustic waves generated by these shear layers interacting with the ambient free-stream are clearly illustrated. The iso-contour of Q-criteria also shows some strong two-dimensional structures near the nozzle lip. These structures are not physical and trigger large acoustic waves which travel to the far-field. This is caused by the DDES models delay in generating three-dimensional turbulent structures, even though it appears to transition to LES mode almost immediately after the nozzle exit. Figure 7 plots a comparison of the shielding function, f_d, and the turbulent eddy viscosity ratio, μ_T/μ_∞, between the DDES model and the RANS-NLES

model with the SEM activated. The shielding function for the DDES simulation appears to stay in RANS mode along the nozzle interior, and then quickly transitions to LES mode just downstream of the nozzle lip. The manually specified shielding function in the RANS-NLES-SEM model also remains in RANS mode in the nozzle interior, but only up to $y^+ \approx 100$, then quickly transitions to LES mode. Comparing the turbulent eddy viscosity ratio, the DDES model retains large eddy viscosity throughout the boundary layer to just past the nozzle exit, while the RANS-NLES-SEM model quickly decays the eddy viscosity after $y^+ = 100$ and only maintains an eddy viscosity ratio of 2 to 4 in the inner portion of the boundary layer.

Figure 8 illustrates the effect of the different turbulence model options and mesh resolution effects. In each of the sub-figures (a) - (d), an iso-contour of the Q-criteria is plotted and colored by stream-wise velocity. Examining the left side of the figure, (a) and (c), a reduction in the delay of generating three-dimensional turbulent structures is observed going from the DDES model to the RANS-NLES model. This is because of the reduced turbulent eddy viscosity in the boundary layer for $y^+ > 100$ using the RANS-NLES model as shown in Figure 7. Once the SEM is activated, this delay is nearly eliminated completely, and all that remains is a quasi-2D waffle cone structure observed at the nozzle exit. Increasing the mesh resolution allows smaller eddies to be resolved inside the nozzle interior which further reduces any two-dimensional or waffle cone like structures at the exit. Figure 9 (a) blanks out the exterior iso-contours of Q allowing the internal jet structure of the RANS-NLES-SEM simulation on the refined grid to be examined. The size of the structures appear too large inside the nozzle, and the structures deep in the boundary layer appear quasi-2D with very little azimuthal variation. This is expected with the relatively coarse circumferential spacing and the use of RANS in the boundary layer. Figure 9 (b) plots the contour of normalized axial velocity at $y^+ \approx 27$ where the RANS model is still activated. The flow appears to be in the early stages of generating resolved three-dimensional structures, but the features are elongated and too highly correlated in both the streamwise and azimuthal directions.

IV.C. Comparison to Experimental Data: Near-Field

Near-field turbulent statistics were computed for the DDES, RANS-NLES, and RANS-NLES-SEM models for comparison with PIV data from the SHJAR.[14] Figure 10 plots the (a) time-average centerline axial velocity, (b) time-averaged lip-line axial velocity, (c) RMS centerline axial velocity, and (d) RMS lip-line axial velocity for each of the simulations and the experimental data. The time-average of the centerline and lip-line velocities agree well with the experiment and little variation is observed between the different hybrid RANS/LES models. Each model appears to capture the length of the potential core and the decay rate of the axial velocity. Examining the RMS of the centerline axial velocity, the comparison to the experiment for the different models remains good. In this case, it appears the RANS-NLES and RANS-NLES-SEM simulations capture the increase in RMS along the centerline up to the length of the potential core slightly better than the DDES model, and the RANS-NLES-SEM performs slightly better than DDES and the RANS-NLES model for the streamwise locations $13 \leq x/D \leq 17$. Much larger differences between the models are observed in the RMS along the lip-line near the nozzle exit. The DDES model grossly over-predicts the axial velocity fluctuations until $x/D \approx 3.5$ which is caused by the large non-physical two-dimensional structures near the nozzle lip. These structures do not appear to be caused by a delay in the shielding function, but from the lack of any resolved turbulent stresses within the nozzle boundary layer. Switching to the RANS-NLES model greatly improves the accuracy of the RMS with a reduction in both the magnitude and extent of the over-prediction. Activating the SEM within the RANS-NLES model further improves the lip-line RMS prediction and a good match to experimental data is observed for $x/D > 1.5$.

There still remains an over-prediction in the lip-line RMS. In order to reduce this over-prediction, physical three-dimensional structures must be resolved in the nozzle boundary layer upstream of the exit. This can be accomplished through further improvements in the mesh, examining the sensitivity to the SEM interface location, and other modeling strategies such as wall-modeled LES in the nozzle interior near the nozzle exit. For example, Bres *et. al.* 7 showed that the lip-line RMS over-prediction at the nozzle exit can be completely removed by simply applying LES using a numerical scheme with almost no dissipation, an explicit sub-grid scale model, and a locally refined mesh in the boundary layer (but still very coarse compared to the suggested wall-resolved LES mesh resolution levels found in the literature). In their simulations, the flow naturally transitioned far upstream of the nozzle exit, and well-developed three-dimensional flow structures are observed within the nozzle. There nozzle geometry was very straight upstream of the exit which lead to a boundary layer $\delta_{99} \approx 0.07$ D based on the experimental data, while the SMC000 geometry converges near the exit and the boundary is 5.5 times smaller than the boundary layer generated using the PPRIME

geometry (based on the RANS result). Inclusion of a wall-model and synthetic turbulence did not appear necessary in there case, the near-field and far-field predictions they reported were very accurate, without these additions. With the significantly smaller boundary layer thickness generated by the SMC000 geometry, a wall-model and synthetic turbulence may be necessary. Evidence of this can be inferred from the results of Ingraham and Bridges,[55] whom used MILES but still observed an over-prediction of the lip-line RMS.

IV.D. Comparison to Experimental Data: Far-Field

Time-accurate volume data from the RANS-NLES-SEM simulation was interpolated onto an acoustic surface triangulation, and propagated to the far-field using the permeable surface Ffowcs Williams-Hawkings (FWH) method within LAVA.[1] The particular formulation of the frequency-domain permeable surface FWH equations used in LAVA is similar to that presented in Lockhard,[56] which was developed for airframe noise propagation. The formulation is equivalent to the one used by Bres *et. al.*[3,7] The one exception is the substitution of the density perturbation with pressure perturbation, $\rho' := \rho_\infty + p'/c_\infty^2$, suggested by Spalart *et. al.*[57] Construction of the FWH surface followed some of the best practices outlined in Bres *et. al.*[3] and Mendez *et. al.*[58] Instead of utilizing end-cap phase averaging to remove spurious contributions from the hydrodynamic fluctuations of the jet, the FWH surface was extended in both the upstream and downstream directions to cover the entire computational domain. It was shown in Ref. 3 that this has the same effect as end-cap averaging, since the coarse mesh and the upwind scheme used for the far-field grids dissipate any hydrodynamic fluctuations. It also greatly simplifies the surface integration process. Figures 11 (a) and (b) plot the permeable FWH surface overlaying a cutting plane of the structured overset grid. The surface contains $312,480$ triangles and the solution is interpolated to the triangle centers using the same tri-linear interpolation routines used for the fringe points in the overset solution algorithm. The far-field propagation utilizes the last $24,000$ time-steps ($24,000\Delta t U_{jet}/D = 148$ convective time-units) of the RANS-NLES-SEM simulation with a sampling rate of every 10 time-steps. This is equivalent to a frequency resolution of $\Delta F = 42$ Hz with a maximum frequency of $F_{max} = 50,000$ Hz. This corresponds to a Strouhal range of $St_{min} = \Delta St \approx 0.007$ to $St_{max} \approx 8$. Following the procedure outlined in Refs. 3 and 7, the total time sample is sub-divided into 5 windows (or segments) with 50 percent overlap, each window has a Strouhal resolution of $\Delta St_{window} = 0.02$. For each time-window a Hanning window (filter) is applied to the time-domain FWH integrands after the mean has been subtracted, then the Fast Fourier Transform (FFT) is applied to transform the integrands into the frequency domain. Windowing (filtering) has the effect of reducing spurious noise at the low frequencies caused by spectral leakage. This is very important for the quieter sideline angles $\phi < 120^o$. Once the FFT is complete, the FWH surface intergrals are evaluated, in the frequency domain, at each observer location to construct the acoustic pressure p'. In the present case of a round jet, 360 observers are azimuthally distributed 100 nozzle diameters from the exit at each of the jet angles $\phi = 60^o$, 90^o, 120^o, and 150^o. During calculation of the PSD, a factor of $\sqrt{8/3}$ is applied to correct for the energy lost from the Hanning window. The PSD is then averaged over the 360 observers for each jet angle, independently for each of the 5 windows. Finally, the 5 windows are averaged and the resulting spectrum is compared to the smooth spectrum of the experimental results (computed over a much larger time-window, i.e. $\Delta St_{exp} = 0.002$) in Figure 12 (a)-(d).

Generally a good agreement is observed in the narrow-band spectrum for each of the directions. The qualitative finding of larger noise generated in the downstream angles and the peak Strouhal frequency is well-captured. An over-prediction in the PSD levels is found for $St > 3.5$. The cause of this is unknown, but may be caused by insufficient dissipation of the NLES model at the higher-wave numbers (i.e. spectral build-up), mesh stretching/aspect ratio effects, or spurious noise from the SEM. Further investigation is necessary to determine the cause. An under-prediction of the low-frequency levels at $\phi = 150^0$ is also observed. The band-limited overall sound pressure level (OASPL) is plotted in Figure 13, where only frequencies associated with $0.08 \leq St \leq 8.0$ are considered. Good agreement is achieved at 120 and 150 degrees where Mach wave radiation is the dominant noise generation mechanism. At the sideline angles of 60 and 90 degrees, where the turbulence in the jet shear layers generates most of the noise, an over-prediction of about 1.8 dB and 1 dB is observed. These are likely caused by the persistence of the quasi-2D waffle cone structures and the associated over-prediction of lip-line RMS near the nozzle exit, as outlined in Ikeda *et. al.*[59] In order to improve these predictions, three-dimensional turbulent structures must be resolved in the boundary layer, upstream of the nozzle exit.[7]

IV.E. *a Posteriori* Error Analysis

In Toosi and Larsson,[60] an *a posteriori* error estimate procedure for anisotropic grid-adaptation of LES was developed. They showed successful application of the approach to wall-resolved LES of fully developed channel flow as well as flow over a backward facing step. The basis of the procedure is to analyze the difference in turbulent kinetic energy using the resolved velocity field with a filtered version of the resolved velocity field. Since the filtering can be performed in each coordinate direction independently, an anisotropic measure of where the mesh should be refined can be estimated. In this work, we follow the approach in Ref. 60 and apply a simple Laplacian filter in each computational coordinate direction to the RANS-NLES-SEM simulation results to construct the filtered velocity field. Time-averaged contours of the estimated unresolved turbulent kinetic energy in each coordinate direction are shown in Figure 14. It is observed that the refined mesh requires further reduction in the axial spacing along the shear layers of the jet from the nozzle exit past the potential core, while the radial spacing appears adequate. The circumferential direction requires the largest resolution increase based on the magnitude of the error estimate, but the region is confined to the shear layer from the nozzle exit to approximately 1.5 D downstream. Examining a close-up view of the circumferential error estimate in Figures 15 (a) and (b), this region is very narrow and starts slightly downstream of the nozzle exit. It is likely that the nozzle exit itself also needs finer azimuthal spacing, but the estimate does not appear to indicate this. With the current overset grid approach, it would be easy to refine the axial spacing and add an additional level of circumferential resolution confined to the local area where the error estimate indicates. An automated procedure for doing this is currently being explored.

V. Summary

The hybrid RANS/LES approach, within the LAVA framework, using structured curvilinear overlapping grids has been applied to the prediction of jet noise and compared to existing near-field PIV and far-field microphone data. Demonstration of the improvements in lip-line RMS prediction with the RANS-NLES-SEM model when compared to the DDES model have been shown. Far-field acoustic predictions of the narrow band PSD compare well to experimental data in both shape in levels. The band limited OASPL in the Mach wave radiation direction also compares well with the data. A small over-prediction of sideline OASPL levels (less than 2 dB), attributed to the over-prediction of lip-line RMS has been observed. Qualitative evidence of this is shown in the quasi-2D waffle cone like structures in the iso-contour of Q-criteria at the nozzle exit. These structures represent a coherent sound source that is not observed in the experimental data, and is a numerical artifact of the simulation. To better capture the lip-line RMS and sideline PSD levels, improvements in the resolution of three dimensional turbulent structures inside the nozzle boundary layer are required. This can be achieved through increased mesh resolution in the axial and circumferential directions, as well as improvements in the modeling of the flow inside the nozzle. For example, the SEM interface can be moved upstream and the RANS-NLES interface can be moved closer to the wall so that the structures have more time develop and eddies closer to the wall can be resolved. Currently, a wall-modeled LES approach, applied locally near the nozzle exit, and utilization of an explicit sub-grid scale model instead of NLES is being explored.

Acknowledgements

This work was funded by the Commercial Supersonics Technology (CST) project under the Advanced Air Vehicles Program (AAVP). Computer time has been provided by the NASA Advanced Supercomputing (NAS) facility at NASA Ames Research Center.

References

[1]Kiris, C., Housman, J., Barad, M., Brehm, C., Sozer, E., and Moini-Yekta, S., "Computational Framework for Launch, Ascent, and Vehicle Aerodynamics (LAVA)," *Aerospace Science and Technology*, Vol. 55, August 2016, pp. 189–219.

[2]Bodony, D. and Lele, S., "Current Status of Jet Noise Predictions Using Large-Eddy Simulation," *AIAA Journal*, Vol. 46, No. 2, 2008, pp. 364–380.

[3]Bres, G., Nichols, J., Lele, S., and Ham, F., "Towards Best Practices for Jet Noise Predictions with Unstructured Large Eddy Simulations," *42nd AIAA Fluid Dynamics Conference, New Orleans, Louisiana*, June 2012, AIAA-2012-2965.

[4]Eastwood, S., Xia, H., and Tucker, P., "Large-Eddy Simulation of Complex Geometry Jets," *Journal of Propulsion and Power*, Vol. 28, No. 2, March-April 2012, pp. 235–245.

[5]Mahak, M., Tyacke, J., and Tucker, P., "Hybrid RANS-NLES of Real Geometry Hot Jets: Flow and Noise Prediction," *52nd AIAA Aerospace Sciences Meeting, National Harbor, Maryland*, January 2014, AIAA-2014-0177.

[6]Tyacke, J., Mahak, M., and Tucker, P., "LES of Jet Flow and Noise with Internal and External Geometry Features," *53rd AIAA Aerospace Sciences Meeting, Kissimmee, Florida*, January 2015, AIAA-2015-0503.

[7]Bres, G., Nichols, J., Lele, S., and Ham, F., "Large Eddy Simulation for Jet Noise: the Importance of Getting the Boundary Layer Right," *21st AIAA/CEAS Aeroacoustics Conference, Dallas, Texas*, June 2015, AIAA-2015-2535.

[8]Mankbadi, R., Lo, S.-C., Lyrintzis, A., Golubev, V., Dewan, Y., and Kurbatskii, K., "Hybrid LES-RANS Simulations of a Jet Impinging on a Flat Plate," *International Journal of Aeroacoustics*, Vol. 15, 2016.

[9]Housman, J. and Kiris, C., "Structured Overlapping Grid Simulations of Contra-Rotating Open Rotor Noise," *54th AIAA Aerospace Sciences Meeting*, January 4-8 2016, AIAA-2016-0814.

[10]Housman, J. and Kiris, C., "Slat Noise Predictions using Higher-Order Finite-Difference Methods on Overset Grids," *22nd AIAA/CEAS Aeroacoustic Conference, Lyon, France*, May 30-31 2016, AIAA-2016-2963.

[11]Brehm, C., Housman, J., and Kiris, C., "Noise Generation Mechanisms for a supersonic jet impinging on an inclined plate," *Journal of Fluid Mechanics*, Vol. 797, 2016, pp. 802–850.

[12]Brehm, C., Housman, J., Kiris, C., and Hutcheson, F., "Noise Characteristics of a Four-Jet Impingement Device Inside a Broadband Engine Noise Simulator," *21st AIAA/CEAS Aeroacoustics Conference, Dallas, Texas*, June 2015, AIAA-2015-2211.

[13]Brown, C. and Bridges, J., "Small Hot Jet Acoustic Rig Validation," Technical Memorandum NASA-TM-2006-214234, National Aeronautics and Space Administration, 2006.

[14]Bridges, J. and Wernet, M., "The NASA Subsonic Jet Particle Image Velocimetry (PIV) Dataset," Technical Memorandum NASA-TM-2011-216807, National Aeronautics and Space Administration, 2011.

[15]Bridges, J., Private Communication.

[16]Steger, J. and Benek, J., "On the Use of Composite Grid Schemes in Computational Aerodynamics," Technical Memorandum 88372, NASA, 1986.

[17]Bogey, C. and Marsden, O., "A Study of the Grid Dependence of the Flow Field and Noise of Subsonic Jets," *54th AIAA Aerospace Science Meeting, San Diego, Ca*, January 2016, AIAA-2016-0261.

[18]Chan, W., "Developments in Strategies and Software Tools for Overset Structured Grid Generation and Connectivity," *20th AIAA Computational Fluid Dynamics Conference, Honolulu, Hawaii*, June 2011, AIAA-2011-3051.

[19]Vinokur, M., "Conservation Equations of Gasdynamics in Curvilinear Coordinate Systems," *Journal of Computational Physics*, Vol. 14, 1974, pp. 105–125.

[20]Spalart, S. and Allmaras, S., "A One-Equation Turbulence Model for Aerodynamic Flows," *30th Aerospace Sciences Meeting and Exhibit, Reno, NV*, January 1992, AIAA-92-0439.

[21]Brehm, C., Barad, M., Housman, J., and Kiris, C., "A Comparison of Higher-Order Finite-Difference Shock Capturing Schemes," *Computers & Fluids*, Vol. 122, November 2015, pp. 184–208.

[22]Shu, C.-W., "High Order Weighted Essentially Nonoscillatory Schemes for Convection Dominated Problems," *SIAM Review*, Vol. 51, No. 1, 2009, pp. 92–126.

[23]Deng, X. and H., Z., "Developing High-Order Weighted Compact Nonlinear Schemes," *Journal of Computational Physics*, Vol. 165, 2000, pp. 22–44.

[24]Vinokur, M. and Yee, H., "Extension of Efficient Low Dissipation High Order Schemes for 3-D Curvilinear Moving Grids," *Frontiers of Computational Fluid Dynamics*, World Scientific, 2002, pp. 129–163, edited by D. A. Caughey and M. M. Hafez.

[25]Deng, X., Mao, M., Tu, G., Liu, H., and Zhang, H., "Geometric Conservation Law and Applications to High-Order Finite Difference Schemes with Stationary Grids," *Journal of Computational Physics*, Vol. 230, 2011, pp. 1100–1115.

[26]Housman, J., Kiris, C., and Hafez, M., "Preconditioned methods for simulations of low speed compressible flows," *Computers & Fluids*, Vol. 38, No. 7, August 2009, pp. 1411–1423.

[27]Housman, J., Kiris, C., and Hafez, M., "Time-Derivative Preconditioning Methods for Multicomponent Flows - Part I: Riemann Problems," *Journal of Applied Mechanics*, Vol. 76, No. 2, February 2009.

[28]Housman, J., Kiris, C., and Hafez, M., "Time-Derivative Preconditioning Methods for Multicomponent Flows - Part II: Two-Dimensional Applications," *Journal of Applied Mechanics*, Vol. 76, No. 3, March 2009.

[29]Deng, X., Mao, M., Jiang, Y., and Liu, H., "New High-Order Hybrid Cell-Edge and Cell-Node Weighted Compact Nonlinear Schemes," *20th AIAA Computational Fluid Dynamics Conference, Honolulu, Hawaii*, June 2011, AIAA-2011-3857.

[30]Nonomura, T. and Fujii, K., "Robust Explicit Formulation of Weighted Compact Nonlinear Scheme," *Computers & Fluids*, Vol. 85, 2013, pp. 8–18.

[31]Thornber, B., Mosedale, A., Drikakis, D., Youngs, D., and Williams, R. J., "An improved reconstruction method for compressible flow with low Mach number features," *Theoretical and Computational Fluid Dynamics*, Vol. 26, 2012, pp. 523–550.

[32]Spalart, S. R., Jou, W.-H., Strelets, M., and Allmaras, S. R., "Comments on the feasibility of LES for wings, and on a hybrid RANS/LES approach," *First AFOSR international conference on DNS/LES, Ruston, Louisiana*, August 1997, Greyden Press.

[33]Strelets, M., "Detached eddy simulation of massively separated flows," *39th Aerospace Sciences Meeting and Exhibit, Reno, Nevada*, January 2001, AIAA-2001-0879.

[34]Spalart, P., Deck, S., Shur, M., Squires, K., Strelets, M., and Travin, A., "A New Version of Detached-Eddy Simulation, Resistant to Ambiguous Grid Densities," *Theoretical and Computational Fluid Dynamics*, Vol. 20, May 2006, pp. 181–195.

[35]Shur, M., Spalart, P. R., Strelets, M., and Travin, A., "A Hybrid RANS-LES Approach with Delayed-DES and Wall-Modelled LES Capabilities," *International Journal of Heat and Fluid Flow*, Vol. 29, 2008, pp. 1638–1649.

[36]Spalart, P. R., "Detached-Eddy Simulation," *Annual Review Fluid Mechanics*, Vol. 41, 2009, pp. 181–202.

[37]Caruelle, B. and Ducros, F., "Detached-Eddy Simulations of Attached and Detached Boundary Layers," *International Journal of Computational Fluid Dynamics*, Vol. 17, 2003, pp. 433–451.

[38]Ashton, N., West, A., and Mendonca, F., "Flow Dynamics Past a 30P30N Three-Element Airfoil Using Improved Delayed Detached-Eddy Simulation," *Journal of Fluid Mechanics*, Vol. 797, 2016, pp. 802–850.

[39]Chauvet, N., Deck, S., and Jacquin, L., "Zonal Detached Eddy Simulation of a Controlled Propulsive Jet," *AIAA Journal*, Vol. 45, No. 10, 2007, pp. 2458–2473.

[40]Deck, S., "Recent Improvements in the Zonal Detached-Eddy Simulation (ZDES) Formulation," *Theoretical and Computational Fluid Dynamics*, Vol. 26, 2012, pp. 523–550.

[41]Shur, M., Spalart, P. R., Strelets, M., and Travin, A., "An Enhanced Version of DES with Rapid Transition from RANS to LES in Separated Flows," *Flow, Turbulence and Combustion*, Vol. 95, No. 4, December 2015, pp. 709–737.

[42]Zhu, H., Fu, S., Shi, L., and Wang, Z., "A Hybrid RANS-Implicit LES Approach for the High-Order FR/CPR Method," *54th AIAA Aerospace Sciences Meeting, San Diego, Ca.*, January 2016, AIAA-2016-1599.

[43]Tucker, P., Eastwood, S., Xia, H., and Loveday, R., "Exploring the LES Model's Role with Jet Noise in Mind," *46th AIAA Aerospace Sciences Meeting and Exhibit, Reno, Nevada*, January 2008, AIAA-2008-527.

[44]Jiang, Y., Mao, M., Deng, X., and Liu, H., "Large Eddy Simulation on Curvilinear Meshes using Seventh-Order Dissipative Compact Scheme," *Computers & Fluids*, Vol. 104, 2014, pp. 73–84.

[45]Uzun, A. and Hussaini, M. Y., "Investigation of High Frequency Noise Generation in the Near-Nozzle Region of a Jet Using Large Eddy Simulation," *Theoretical and Computational Fluid Dynamics*, Vol. 21, 2007, pp. 291–321.

[46]Aikens, K., Dhamankar, N., Martha, C., Situ, Y., Blaisdell, G., Lyrintzis, A., and Li, Z., "Equilibrium Wall Model for Large Eddy Simulations of Jets for Aeroacoustics," *52nd AIAA Aerospace Sciences Meeting, National Harbor, Maryland*, January 2014, AIAA-2014-0180.

[47]Aikens, K., Blaisdell, G., and Lyrintzis, A., "Analysis of Converging-Diverging Beveled Nozzle Jets Using Large Eddy Simulation with a Wall Model," *53rd AIAA Aerospace Sciences Meeting, Kissimmee, Florida*, January 2015, AIAA-2015-0509.

[48]Jarrin, N., Benhamadouche, S., Laurence, D., and Prosser, R., "A Synthetic-Eddy-Method for Generating Inflow Conditions for Large-Eddy Simulations," *International Journal of Heat and Fluid Flow*, Vol. 27, 2006, pp. 585–593.

[49]Jarrin, N., Prosser, R., Uribe, J.-C., Benhamadouche, S., and Laurence, D., "Reconstruction of Turbulent Fluctuations for Hybrid RANS/LES simulations using a Synthetic-Eddy Method," *International Journal of Heat and Fluid Flow*, Vol. 30, 2009, pp. 435–442.

[50]Shur, M., Spalart, P., Strelets, M., and Travin, A., "Synthetic Turbulence Generators for RANS-LES Interfaces in Zonal Simulations of Aerodynamic and Aeroacoustic Problems," *Flow Turbulence and Combustion*, Vol. 93, 2014, pp. 63–92.

[51]Shur, M., Spalart, P. R., and Strelets, M., "Noise prediction for increasingly complex jets, Part 1 Methods and Tests," *International Journal of Aeroacoustics*, Vol. 4, 2005, pp. 213–246.

[52]Shur, M., Spalart, P. R., and Strelets, M., "Noise prediction for increasingly complex jets, Part 2 Applications," *International Journal of Aeroacoustics*, Vol. 4, 2005, pp. 247–266.

[53]Georgiadis, N., Rizzetta, D., and Fureby, C., "Large-Eddy Simulation: Current Capabilities, Recommended Practices, and Future Research," *47th AIAA Aerospace Sciences Meeting, Orlando, Florida*, January 2009, AIAA-2008-948.

[54]Larsson, J., Kawai, S., Bodart, J., and Bermejo-Moreno, I., "Large Eddy Simulation with Modeled Wall-Stress: Recent Progress and Future Directions," *J-STAGE*, 2015.

[55]Ingraham, D. and Bridges, J., "Validating a Monotonically-Integrated Large Eddy Simulation Code for Subsonic Jet Acoustics," *55th AIAA Aerospace Sciences Meeting, Grapevine, Texas*, January 2017, AIAA-2017-0456.

[56]Lockard, D., "A Comparison of Ffowcs Williams-Hawkings Solvers for Airframe Noise Applications," *8th AIAA/CEAS Aeroacoustics Conference & Exhibit, Breckenridge, Colorado*, June 2002, AIAA-2002-2580.

[57]Spalart, P. R. and Shur, M., "Variants of the Ffowcs Williams-Hawkings Equation and their Coupling with Simulations of Hot Jets," *International Journal of Aeroacoutics*, Vol. 8, No. 5, 2009, pp. 477–492.

[58]Mendez, S., Shoeybi, M., Lele, S., and Moin, P., "On the use of the Ffowcs Williams-Hawkings Equation to Predict Far-Field Jet Noise from Large Eddy-Simulations," *International Journal of Aeroacoustics*, Vol. 12, 2013.

[59]Ikeda, T., Enomoto, S., Yamamoto, K., and Amemiya, K., "On the Modification of the Ffowcs Williams-Hawkings Integration for Jet Noise Prediction," *19th AIAA/CEAS Aeroacoustics Conference, Berlin, Germany*, May 2013, AIAA-2013-2277.

[60]Toosi, S. and Larsson, J., "Anisotropic Grid-Adaptation in Large Eddy Simulations of Wall-Bounded and Free Shear Flows," *55th AIAA Aerospace Science Meeting, Grapevine, Tx.*, January 2017, AIAA-2017-0978.

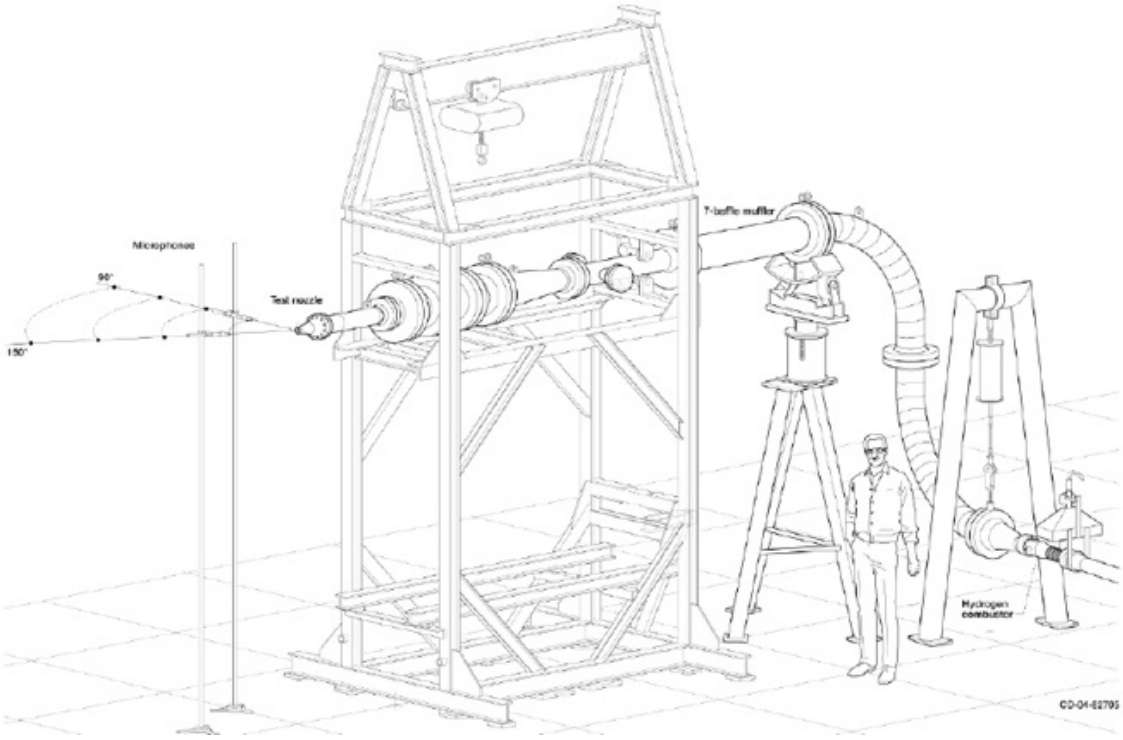

Figure 1. Perspective view of a schematic of the Small Hot Jet Acoustic Rig (SHJAR) located in the Aeroacoustic Propulsion Laboratory (AAPL) at the NASA Glenn Research Center.

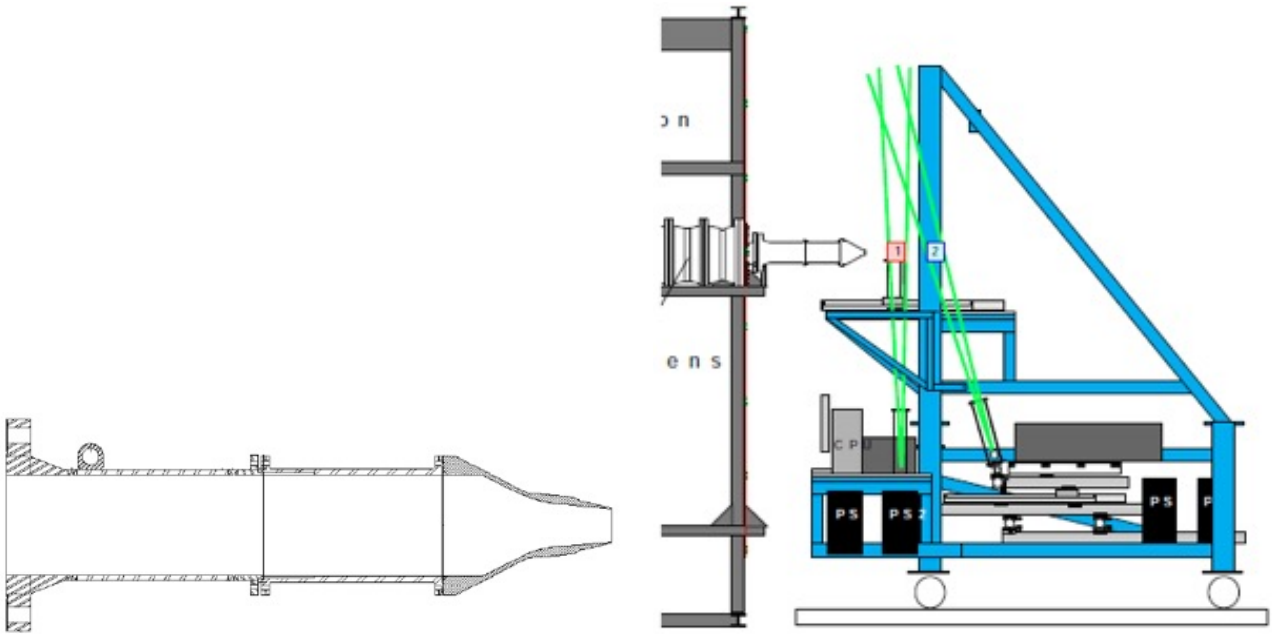

(a) Nozzle (b) PIV

Figure 2. (a) Drawing of the baseline axisymmetric convergent Small Metal Chevron (SMC000) nozzle. (b) Drawing of the PIV measurement device illustrating the PIV planes (shown in green) and their orientation to the nozzle.

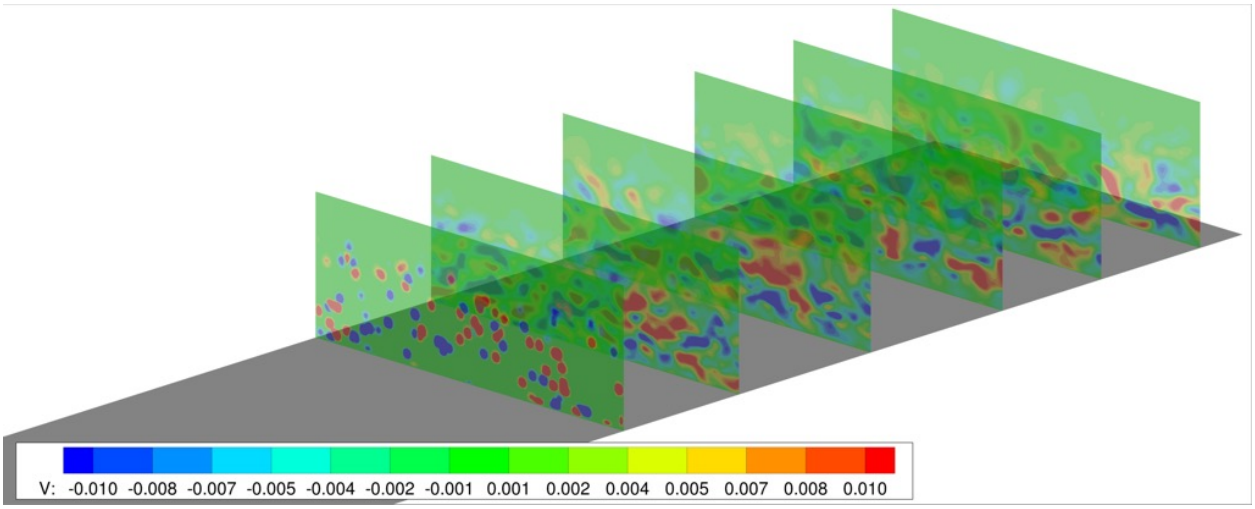

(a) Instantaneous span-wise velocity

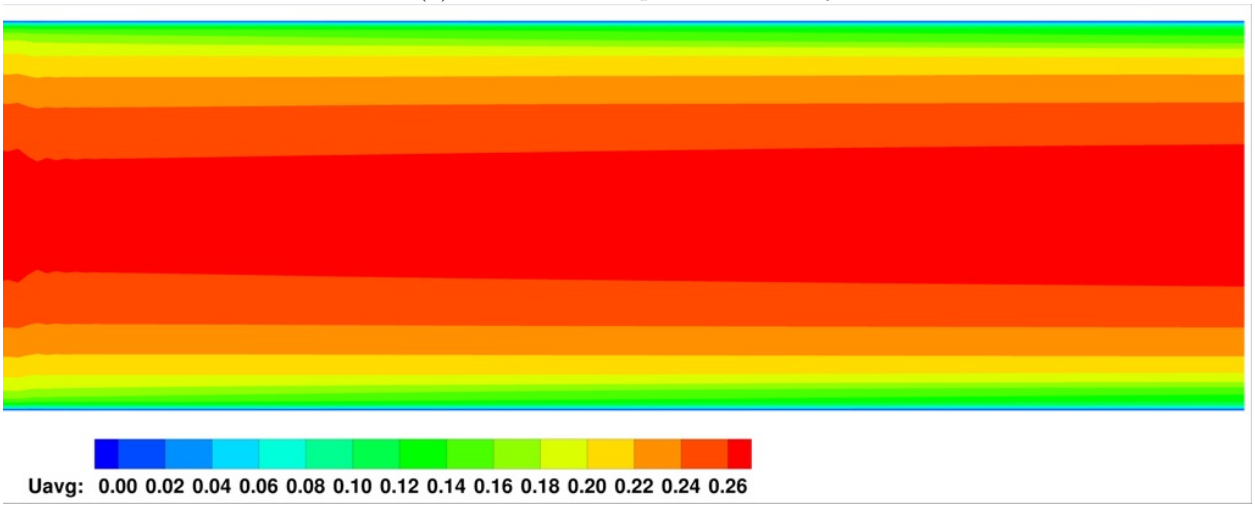

(b) Time-averaged stream-wise velocity

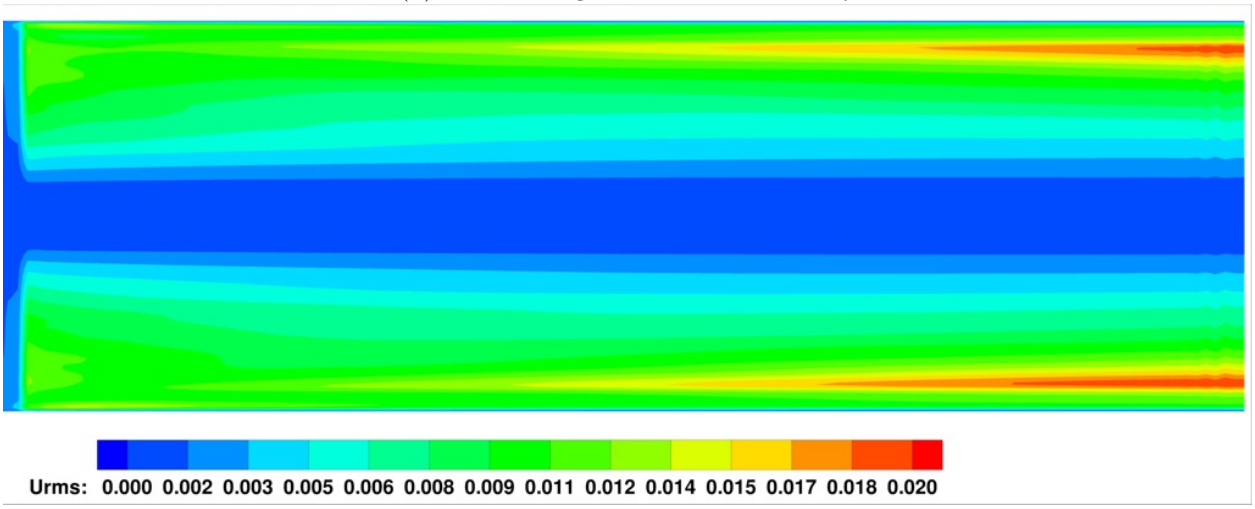

(c) RMS stream-wise velocity

Figure 3. (a) Isometric view of the instantaneous span-wise velocity illustrating the synthetic eddies inserted into the channel flow at the first plane, and their evolution downstream. (b) Time-averaged stream-wise velocity showing a small perturbation in the boundary layer where the synthetic eddies are inserted and the recovery of the boundary layer downstream. (c) RMS stream-wise velocity showing the development of the resolved turbulent content downstream of the SEM interface.

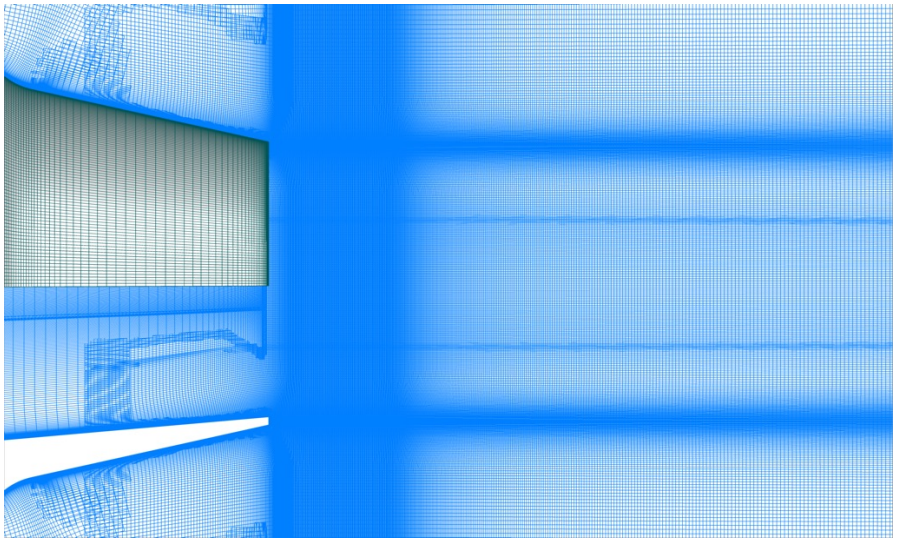

(a) Baseline (256M)

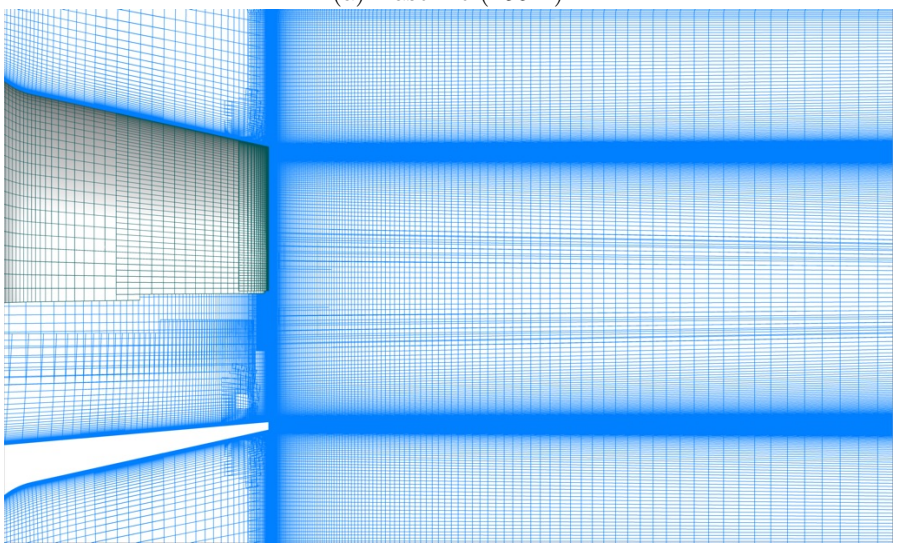

(b) Coarse (28M)

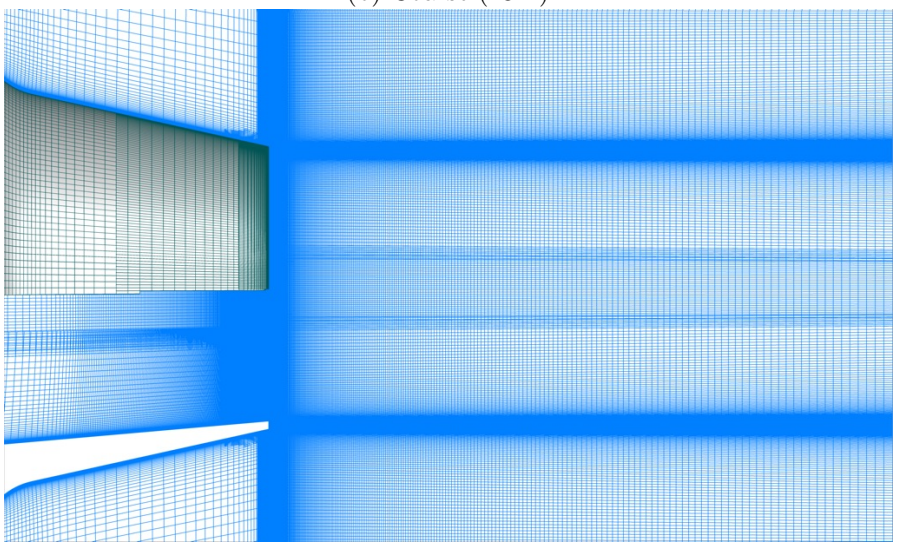

(c) Refined (106M)

Figure 4. A cutting plane through the jet centerline along (shown in blue) with the upper half of the nozzle surfaces (shown in green) of the structured overlapping grid systems (a) baseline, (b) coarse, and (c) refined. Note the bottom half of the nozzle surface grids have been suppressed to allow the nozzle interior grid to be shown.

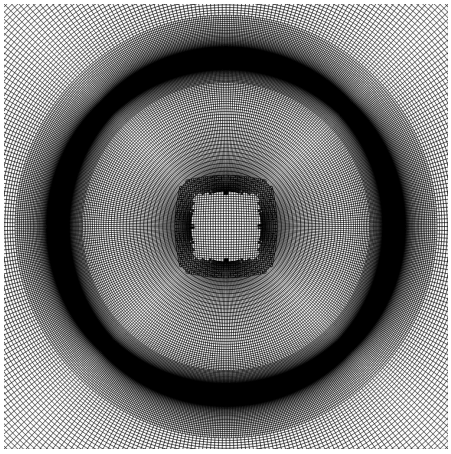

Figure 5. An streamwise cutting plane of the refined structured overlapping grid system illustrating the radial variation in circumferential spacing and the core grid generated to remove the axis singularity.

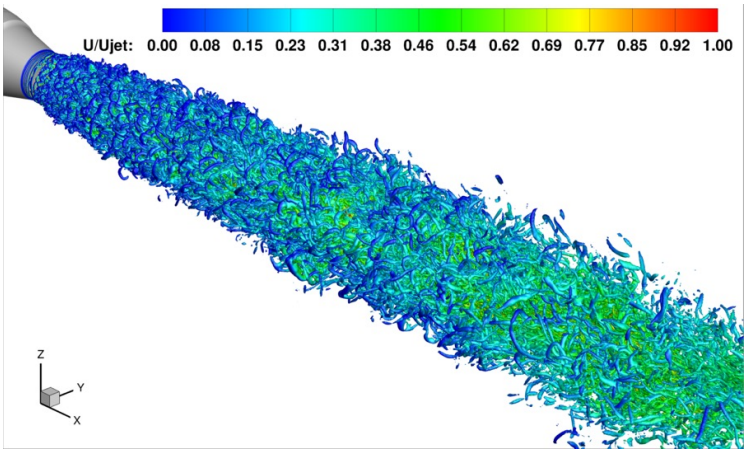

(a) Instantaneous Q-criteria

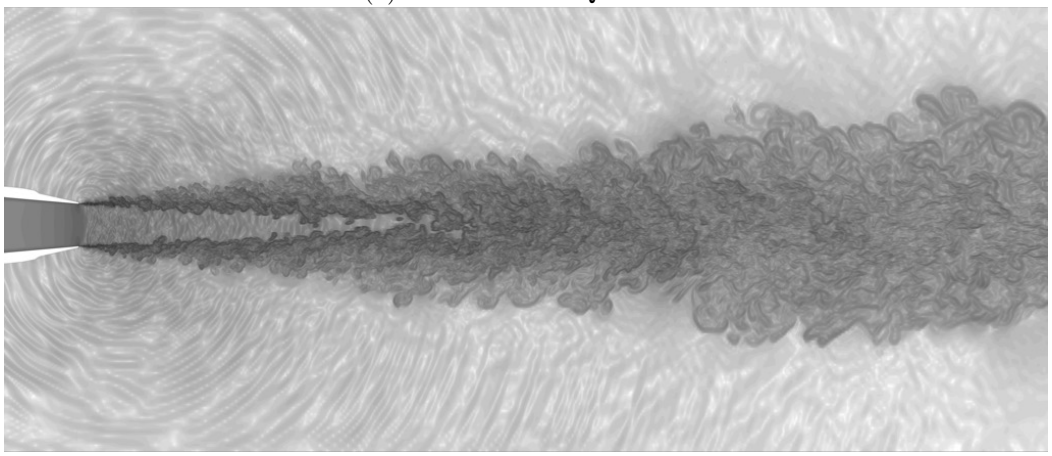

(b) Instantaneous Magnitude of the Density Gradient

Figure 6. Instantaneous flow-field images of the (a) Q-criteria colored by normalized axial velocity and (b) magnitude of the density gradient showing the resolved three-dimensional turbulent structures and the acoustic waves propagating to the far-field using the DDES model on the baseline grid.

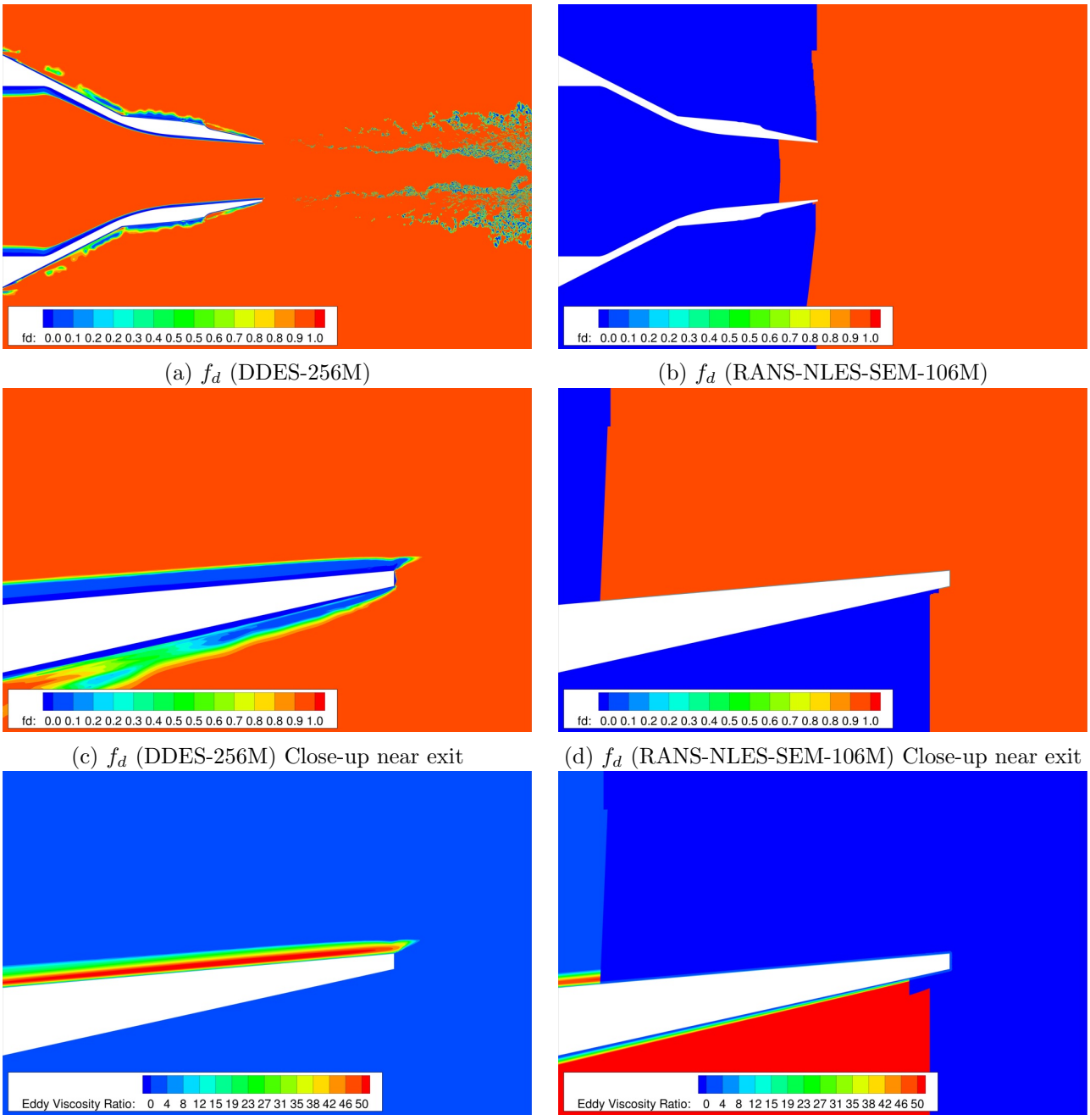

(a) f_d (DDES-256M)

(b) f_d (RANS-NLES-SEM-106M)

(c) f_d (DDES-256M) Close-up near exit

(d) f_d (RANS-NLES-SEM-106M) Close-up near exit

(e) μ_T/μ_∞ (DDES-256M)

(f) μ_T/μ_∞ (RANS-NLES-SEM-106M)

Figure 7. Comparison images of the two hybrid RANS/LES models used in the simulations; (left) DDES and (right) RANS-NLES-SEM; (a-b) showing the shielding function, (c-d) f_d, and (e-f) the turbulent eddy viscosity ratio, μ_T/μ_∞

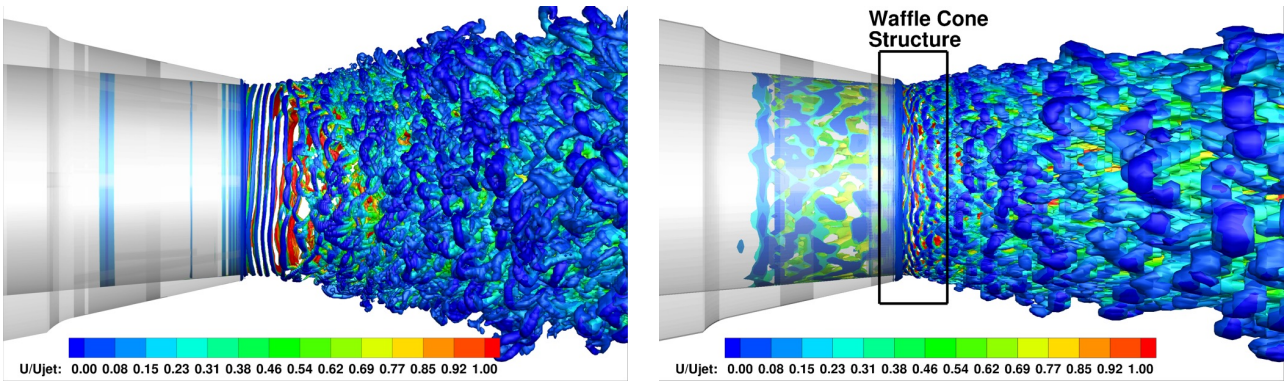

(a) DDES (256M) (b) RANS-NLES-SEM (28M)

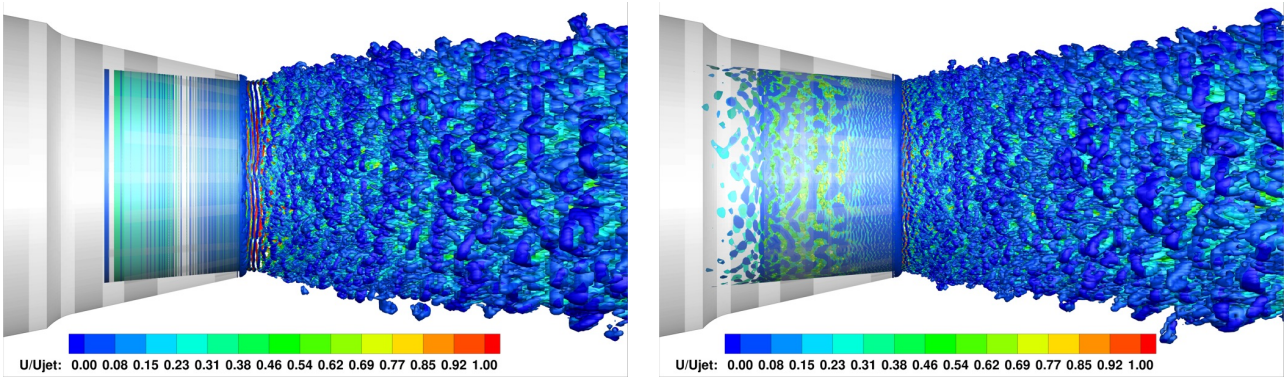

(c) RANS-NLES (106M) (d) RANS-NLES-SEM (106M)

Figure 8. Comparison of iso-contour of Q-criteria colored by normalized axial velocity for (a) DDES on the baseline mesh, (b) RANS-NLES-SEM on the coarse mesh, (c) RANS-NLES on the refined mesh, and (d) RANS-NLES-SEM on the refined mesh. Quasi-2D waffle cone like structure is indicated by the rectangular box near the nozzle exit.

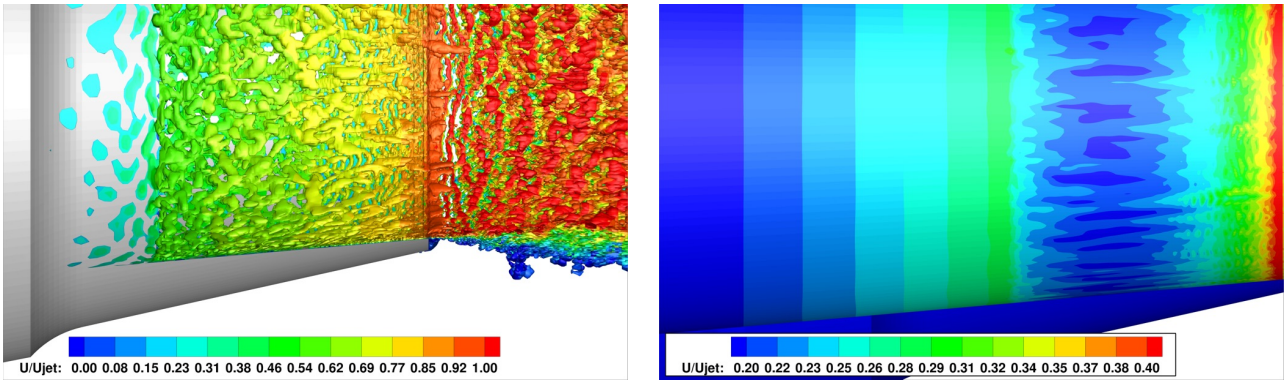

(a) (b)

Figure 9. (a) Iso-contour of Q-criteria colored by normalized axial velocity using the RANS-NLES-SEM model on the refined mesh with the exterior iso-contour blanked out. (b) Normalized axial velocity contour on the nozzle interior at $y^+ \approx 27$.

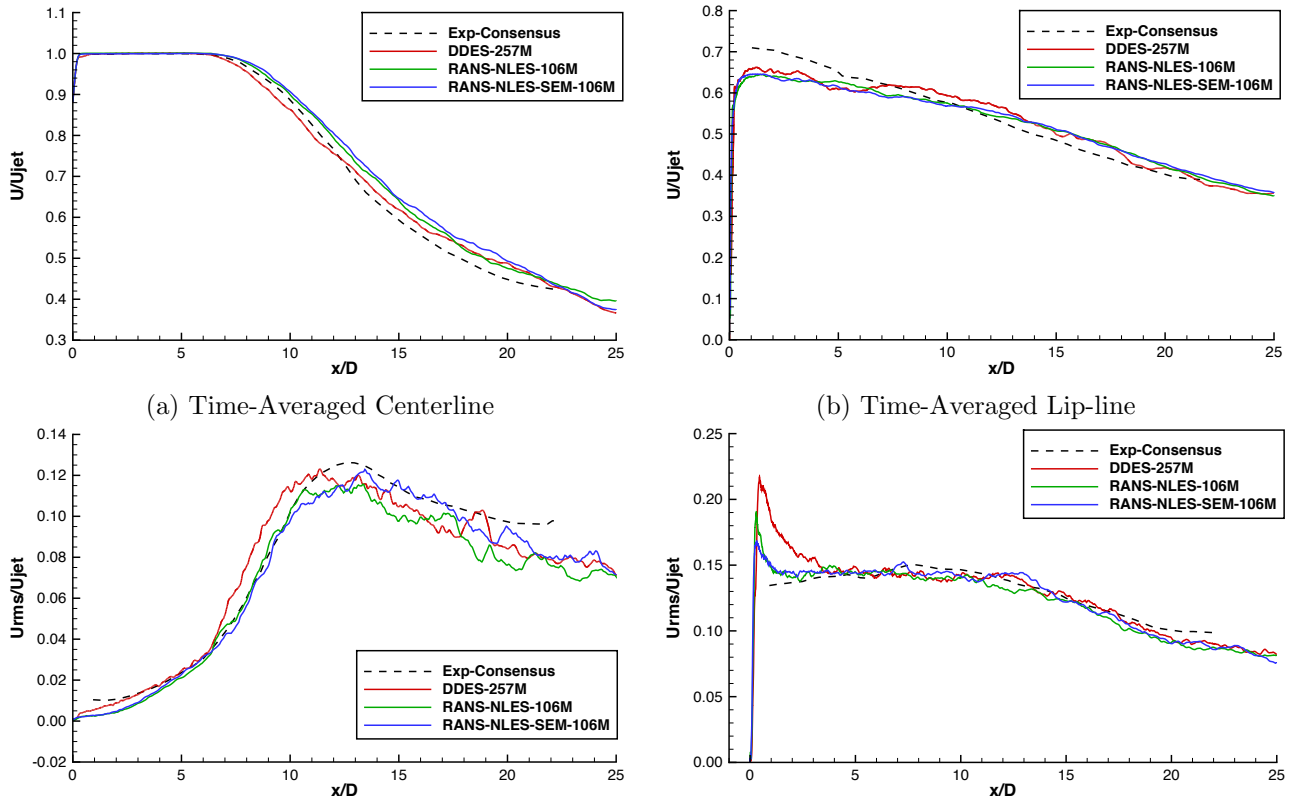

(a) Time-Averaged Centerline

(b) Time-Averaged Lip-line

(c) RMS Centerline

(d) RMS Lip-line

Figure 10. Comparison of turbulent axial velocity statistics between the two hybrid RANS/LES models and the experiment for the (a) time-averaged centerline, (b) time-averaged lip-line, (c) RMS centerline, and (d) RMS lip-line.

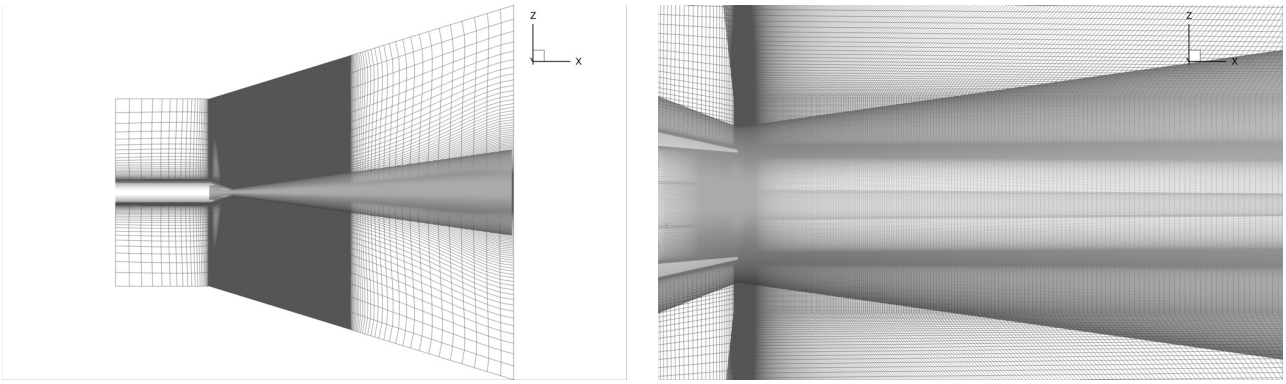

(a) Global View

(b) Close-up View

Figure 11. Permeable Ffowcs Williams-Hawkings (FWH) surface (translucent) overlaying a cutting plane of the structured overset grid.

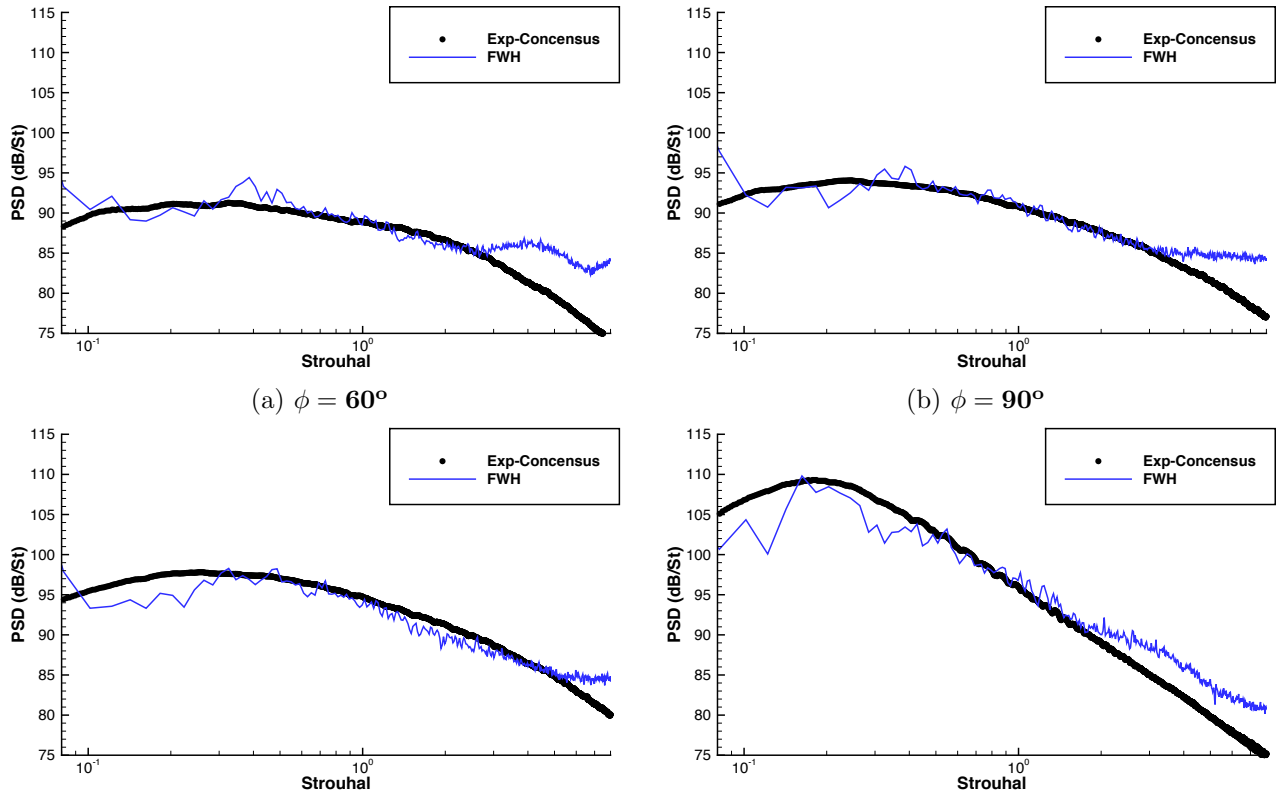

(a) $\phi = \mathbf{60^o}$ (b) $\phi = \mathbf{90^o}$

(c) $\phi = \mathbf{120^o}$ (d) $\phi = \mathbf{150^o}$

Figure 12. Comparison between the experimental consensus and the FWH propagation of the RANS-NLES-SEM simulation for the far-field power spectral density (PSD) at 100 D and (a) $\phi = 60^o$, (b) $\phi = 90^o$ (c) $\phi = 120^o$ (d) and $\phi = 150^o$.

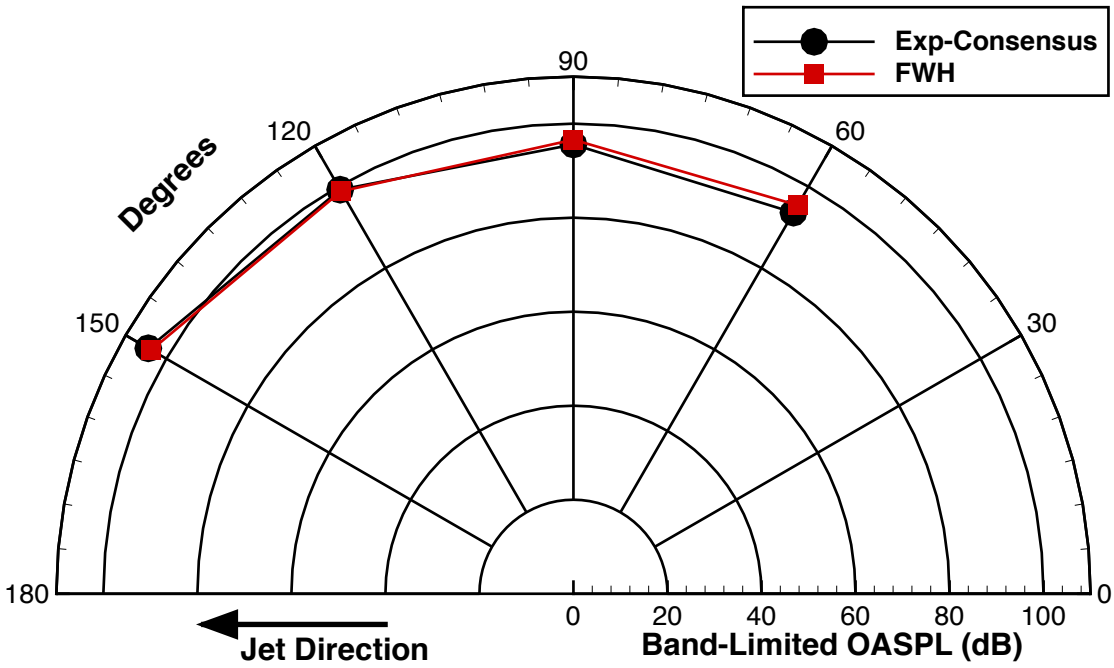

Figure 13. Band limited ($0.08 < St < 0.8$) overall sound pressure levels at 50D from the nozzle exit, comparing the experiment and the FWH propagation of the RANS-NLES-SEM simulation.

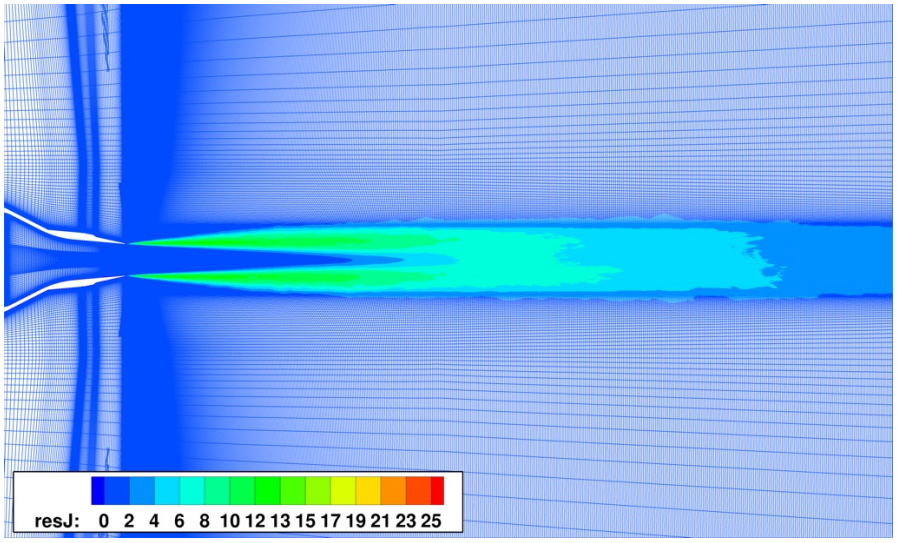

(a) Axial

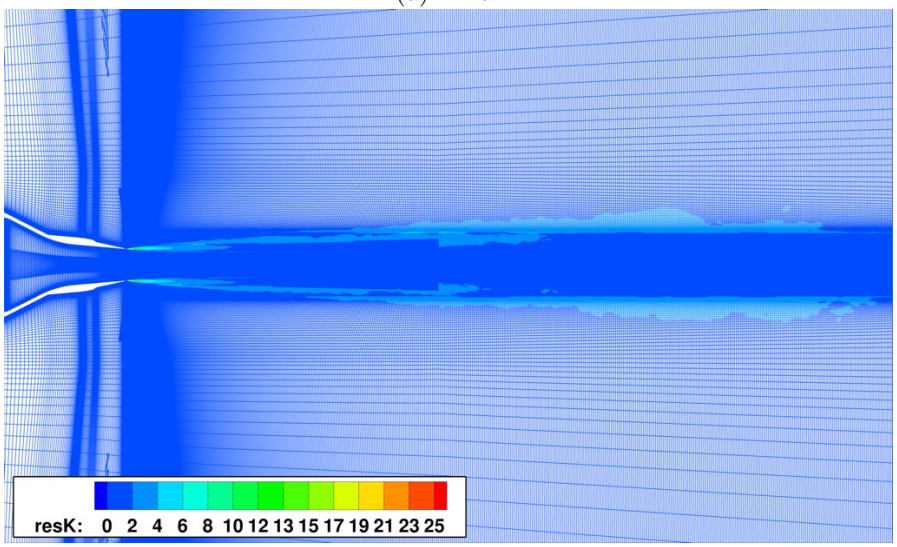

(a) Circumferential

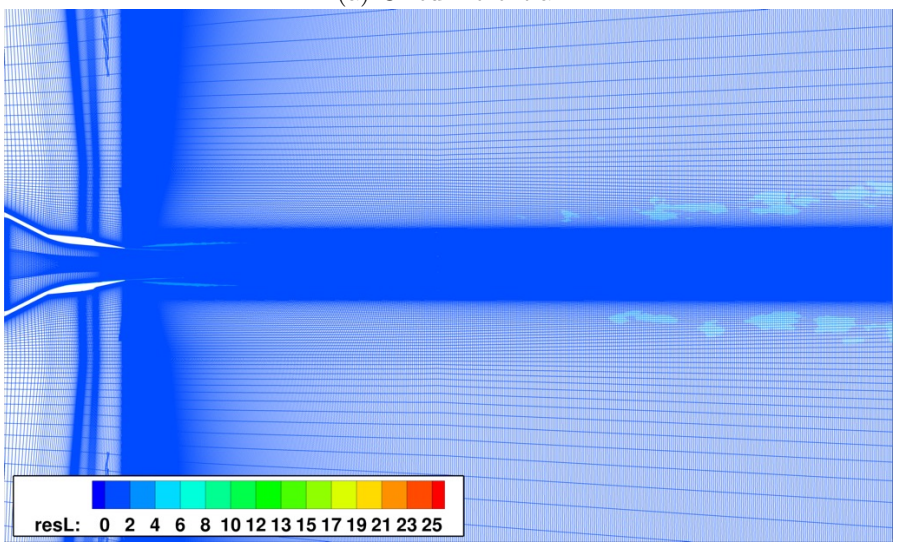

(a) Radial

Figure 14. Mesh colored by countour values of the *a posteriori* error estimate of the unresolved turbulent kinetic energy in the (a) axial, (b) circumferential, and (c) radial directions

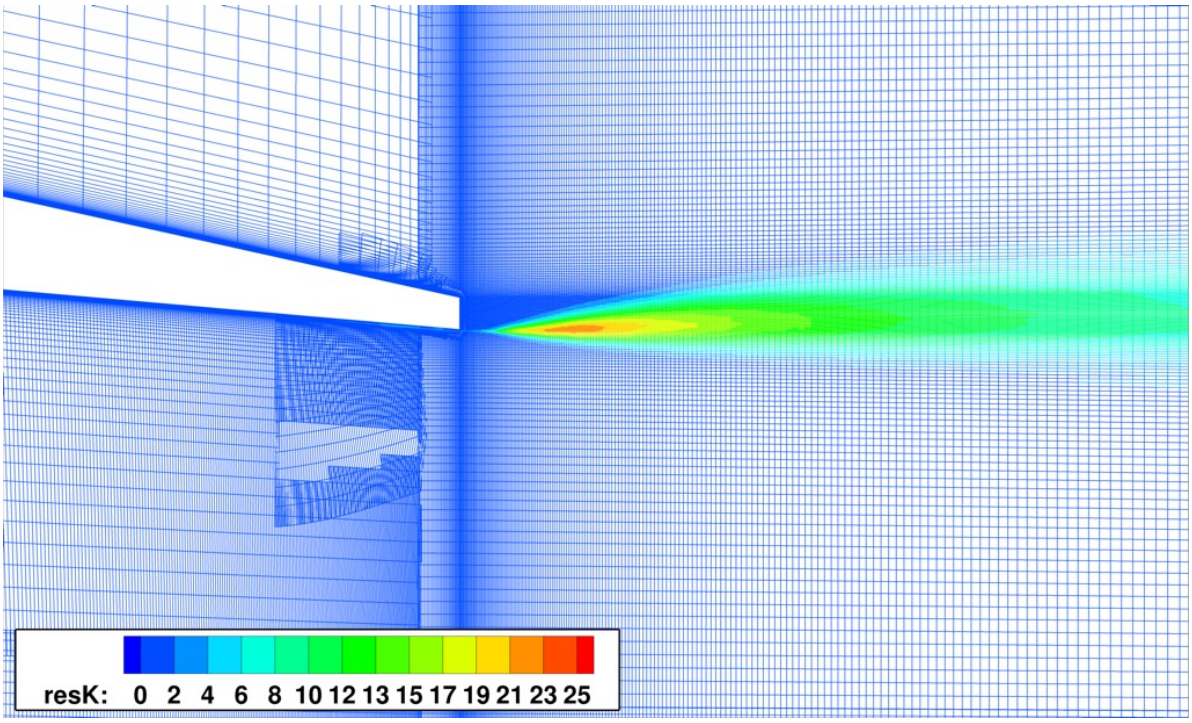

(a)

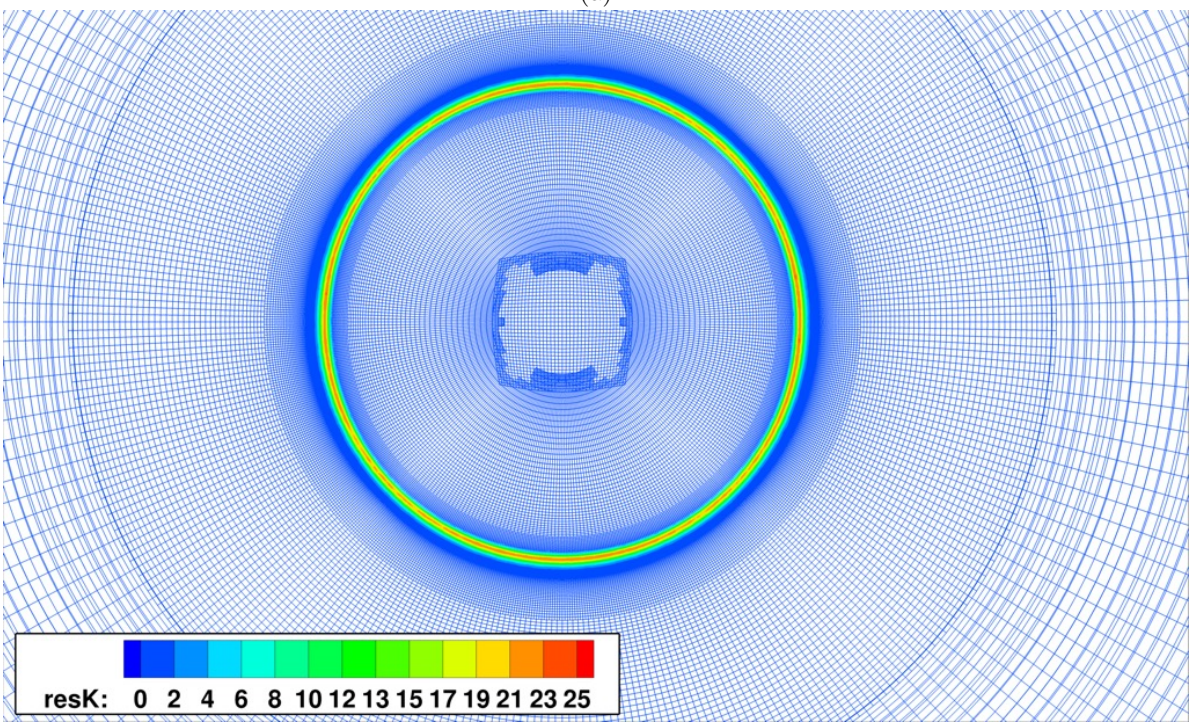

(b)

Figure 15. Close-up views of the mesh colored by contours values of the *a posterior* error esimate of the unresolved turbulent kinetic energy in the circumferential spacing on (a) a slice through the jet and (b) a streamwise cutting plane near the maximum.